

A Comprehensive Analysis of Macrosegregation Formation During Twin-Roll Casting



CHRISTIAN M.G. RODRIGUES, ANDREAS LUDWIG, MENGHUAI WU,
ABDELLAH KHARICHA, and ALEXANDER VAKHRUSHEV

A two-phase Eulerian–Eulerian volume-averaged model is used to predict the formation of macrosegregation during the twin-roll casting of inoculated Al-4 wt pct Cu alloys. For low solid fractions, the equiaxed crystals are modeled according to the submerged object approach. However, above a given transition limit, they are assumed to behave like a viscoplastic material. This means that the solid phase behaves as a coherent structure that can influence the motion of the liquid. Such approach allows one to take into account the flow dynamics arising from the occurrence of both solidification and hot rolling simultaneously, which usually occurs in twin-roll casting. Therefore, it is possible to explain the origin of the macrosegregation patterns obtained in the simulations based on the relative motion between the phases. Compression-induced expulsion of segregated melt is observed as a result of the deformation of the solidifying shells. Such occurrence leads to a negative macrosegregation region in the outer part of the as-cast strip. Then, because the solute-enriched melt is squeezed out toward adjacent regions, two positively segregated bands can be found near the center of the domain. Furthermore, it is shown how solidification-induced feeding weakens the absolute value of the negative and positive segregation bands.

<https://doi.org/10.1007/s11663-019-01527-x>
© The Author(s) 2019

I. INTRODUCTION

MACROSEGREGATION is a term that denotes a concentration inhomogeneity at the scale of a casting. It poses a severe quality issue for big ingots or continuously cast slabs. It is generally believed that the smaller the dimension of a casting the less distinctive are macrosegregations. This opinion is motivated by the fact that in most cases, the relative motion between solute-enriched liquid and solute-depleted crystals necessary for the formation of macrosegregation is caused by (i) natural or forced convection, (ii) sedimentation of crystals, and/or (iii) solidification-induced feeding flow.^[1–4] However, if deformation during solidification is the main reason for the relative motion between solid

and liquid, then one can conclude that macrosegregation can also form in thin products such as in sheets produced by twin-roll casting.

Twin-roll casting is a technology that has been used over the recent decades for commercial production of thin metal strips. During this process, the molten metal is injected into the gap between two water-cooled counter-rotating rolls. As a result, it solidifies and the corresponding solid shell that forms on each of the moving roll surfaces is subjected to a considerable amount of hot rolling before reaching the roll nip.

This technology has many advantages compared with conventional casting techniques. The major advantage has to do with the reduced number of operational steps in the production line. This leads to a reduction in investment and processing costs, as well as less-rigorous logistics and labor requirements.^[5,6] According to Barekar and Dhindaw,^[7] it also yields fewer greenhouse gas emissions. Furthermore, due to the very high cooling rates, the final strand is expected to have a refined microstructure with improved mechanical properties.^[8,9]

On the other hand, combining metal solidification with hot rolling into one single step makes it more sensitive to process conditions,^[10] and eventually susceptible to a number of casting defects.^[11–14] In fact, over the years, as the emphasis has been growing for

CHRISTIAN M. G. RODRIGUES, ANDREAS LUDWIG, and MENGHUAI WU are with the Metallurgy Department, Montanuniversität Leoben, Franz-Josef Street 18, 8700 Leoben, Austria, Contact e-mail: christian.gomes-rodrigues@unileoben.ac.at ABDELLAH KHARICHA is with the Metallurgy Department, Montanuniversität Leoben and also with the Christian-Doppler Laboratory for Metallurgical Application of Magnetohydrodynamics, Montanuniversität Leoben, Franz-Josef Street 18, 8700 Leoben, Austria. ALEXANDER VAKHRUSHEV is with the Christian-Doppler Laboratory for Metallurgical Application of Magnetohydrodynamics, Montanuniversität Leoben.

Manuscript submitted December 03 2018.

Article published online February 19, 2019.

improving productivity, increasing attention has been placed on the understanding of the corresponding complex melt flow and solidification patterns.

The behavior of metallic alloys in the semisolid state is complex as it has been found that its behavior changes dramatically as the solid fraction increases. For flows with very dilute solid particles, the viscosity of the mixture is usually dependent on the solid fraction and the liquid viscosity. As the solid fraction increases, at specifically above a certain level (hereafter referred as transition solid fraction), the material develops a considerable resistance to deformation,^[15] usually reflected by an abrupt increase in the viscosity field.

In view of the above reason, many research groups in this field simply assume that, at this stage, the mixture behaves as a fixed, rigid solid body. For instance, Ni and Beckermann^[16] suggested a volume-averaged two-phase model which described the transport phenomena during solidification. Based on this pioneering numerical model, other studies ensued by applying the concept to equiaxed,^[17] columnar,^[18–20] and the most general columnar/equiaxed^[21] solidification.

However, although valuable progress has been achieved in the simulation of transport of crystals, the assumption of fixed rigid solid body for large solid fractions is still an oversimplification of the general solidification process (as pointed out above). Furthermore, another drawback of such concept is that it is only valid when the solid particles are entirely surrounded by liquid. This assumption allows one to consider that the pressure at the solid–liquid interface can be approximated by the average liquid pressure, and finally results in one single pressure field for both phases. This is a key point that greatly simplifies the solution procedure, and it is an important reason as to why it is so popular in the metallurgical community. However, it should be fairly reasonable to say that such conditions are not usually fulfilled in most industrial applications.

On the other hand, a more complex description of the semisolid slurry is to treat it as a viscoplastic continuous solid skeleton saturated with interstitial liquid.^[22] Such a state is characterized by a continuous coherent structure that is able to sustain significantly higher stresses. In this case, the macroscopic velocity gradients in the solid can no longer be neglected since the deformation and motion of the skeleton is now strictly connected to the hydrodynamic properties of the liquid flow. In fact, under these circumstances, solid and liquid phases become inherently coupled: if, on the one hand, pressing the solid skeleton drives the fluid flow behavior, on the other, the resulting pressure distribution in the interstitial liquid affects the equivalent stress experienced by the solid phase.

Suéry and his team had a substantial contribution in this field by analyzing the rheological and mechanical behavior of alloys,^[22–24] and by proposing constitutive equations for viscoplastic porous metallic materials saturated with liquid.^[25,26] Based on the investigation of the mechanical behavior of an aluminum alloy in the semisolid state, Nguyen *et al.*^[22] suggested that the onset of the viscoplastic behavior occurs at a solid fraction of 57 pct. Similarly, Fachinotti *et al.*^[27] developed a

thermomechanical and macrosegregation model for solidification of binary alloys. Contrary to the previous models, the one detailed in Fachinotti *et al.*^[27] is not limited to isothermal conditions as the authors were able to consider the mass transfer between phases. This feature makes it applicable to actual solidification processes.

Regarding specifically scenarios replicating twin-roll casting, one can find that it is usually done by using single phase finite element codes, originally designed for pure rolling, and by treating the liquid as a solid with low viscosity.^[28,29] On the other hand, if a liquid core still exists at the roll nip, an approximate solution can be achieved by neglecting the mechanical framework in the model.^[30] However, the viscoplasticity of the semisolid slurry must be considered if solidification has already reached the strand center before reaching the roll nip. In fact, this scenario is a great example where the deformation of the semisolid metallic alloy plays an important role in the outcome of the process, and therefore, in this case the viscoplastic regime should not be ignored.

The current study is an attempt to fill this gap that still prevails in the research community regarding the solidification process, and particularly when the material is then subjected to imposed deformation. A stand-alone numerical model has been developed to account for the transport and growth of equiaxed crystals during solidification. Furthermore, in order to account for mush deformation, a solution algorithm has been developed to include a viscoplastic regime when the concentration of solid is above the transition solid fraction. The model is implemented in OpenFOAM and is applied to a test case replicating a twin-roll casting process.

II. MODEL DESCRIPTION

In the current study, the simulation of the twin-roll casting relies on a two-phase Eulerian–Eulerian volume-averaged model. This approach solves mass, momentum, species, and enthalpy conservation equations for both phases. The two phases considered here are the liquid melt (ℓ) and the solid equiaxed crystals (s), with the sum of their volume fractions being always equal to unity. Furthermore, the model also takes into account a transport equation for the grain number density, with a predetermined value being assumed at the beginning of the simulation. Conservation equations, sources terms, and auxiliary equations are summarized in Table I with the subscript i referring to one of the two phases. Note that when $i = \ell$, the minus sign from “ \mp ” must be taken, whereas when $i = s$ the parameter in question is positive. In any case, all the parameters are properly identified in the nomenclature section. Further assumptions include neglecting the effect of gravity, and considering constant density fields in both phases.

All quantities are volume averaged in the present formulation, although they are not distinguished as such in Table I. This compromise on the detail of the equations is expected to facilitate the reading process.

Table I. Volume-Averaged Conservation Equations

Mass Cons.:	$\frac{\partial g_i \rho_i}{\partial t} + \nabla \cdot (g_i \rho_i \mathbf{v}_i) = \mp M_{ls}$	(11)
Momentum Cons.:	$\frac{\partial g_i \rho_i \mathbf{v}_i}{\partial t} + \nabla \cdot (g_i \rho_i \mathbf{v}_i \mathbf{v}_i) = -g_i \nabla p + \nabla \cdot g_i \boldsymbol{\tau}_i^{\text{eff}} \mp \mathbf{U}_{ls}$	(12)
Species Cons.:	$\frac{\partial g_i \rho_i c_i}{\partial t} + \nabla \cdot (g_i \rho_i \mathbf{v}_i c_i) = \nabla \cdot (g_i \rho_i D_i \nabla c_i) \mp C_{ls}$	(13)
Enthalpy Cons.:	$\frac{\partial g_i \rho_i h_i}{\partial t} + \nabla \cdot (g_i \rho_i \mathbf{v}_i h_i) = -\nabla \cdot \left(\frac{\lambda_i}{c_{pi}} \nabla h_i \right) \mp H_{ls}$	(14)
Grain Transport:	$\frac{\partial n}{\partial t} + \nabla \cdot (\mathbf{v}_s n) = 0$	(15)

From the set of conservation equations, one can realize that the solid phase is treated in a very similar manner as the liquid. The major distinction has to do with how the deviatoric stress term presented in the momentum equations should be expressed. For the liquid phase, it is assumed that it behaves as an incompressible Newtonian fluid and so the viscous stress is proportional to the deviatoric part of the strain rate:

$$\boldsymbol{\tau}_l^{\text{eff}} = \boldsymbol{\tau}_l = 2\mu_l \text{dev}(\dot{\boldsymbol{\epsilon}}_l), \quad [1]$$

where the strain rate tensor is given by $\dot{\boldsymbol{\epsilon}}_l = 1/2(\nabla \mathbf{v}_l + (\nabla \mathbf{v}_l)^T)$ and the liquid viscosity is assumed to be constant ($\mu_l = 0.013 \text{ Pa} \cdot \text{s}$). Note that the flow is assumed to be laminar in the present model. Considering that the characteristic size L (casting size) in the domain is 0.01 m, and the corresponding liquid velocity is 0.04 m/s, the system Reynolds number ($\text{Re} = L \mathbf{v}_l \rho_l / \mu_l$) is about 80, which is less than the critical number 2100 for the onset of turbulence flow.

As for the solid phase, the deviatoric stress term will depend on the volume fraction in the region under consideration. In fact, whether the semisolid lies within the viscoplastic regime or not will influence the solution procedure. Below the viscoplastic threshold (g_s^t), the approach is similar to the liquid phase, even though the viscosity is no longer kept constant throughout the regime (as shown below). On the other hand, as the solid fraction increases above g_s^t , the mechanical properties of the solid phase change dramatically, and the behavior of the solid phase has been modeled according to a compressible viscoplastic model.^[22] Combining both approaches into a general mathematical statement yields:

$$\boldsymbol{\tau}_s^{\text{eff}} = \begin{cases} 2\mu_s \text{dev}(\dot{\boldsymbol{\epsilon}}_s) & \text{for } g_s \leq g_s^t \\ 2\frac{\mu_s^{\text{app}}}{A} \text{dev}(\dot{\boldsymbol{\epsilon}}_s) + \mu_s^{\text{app}} \left(\frac{1}{9B} \right) \text{tr}(\dot{\boldsymbol{\epsilon}}_s) \mathbf{I} & \text{for } g_s > g_s^t \end{cases} \quad [2]$$

where $\dot{\boldsymbol{\epsilon}}_s = 1/2(\nabla \mathbf{v}_s + (\nabla \mathbf{v}_s)^T)$.

Comparison between the equations defined for each regime in Eq. [2] suggests that the first term in the viscoplastic regime ($g_s > g_s^t$) is somewhat analogous to the viscous stress defined in the lower solid fraction range ($g_s \leq g_s^t$), with the corresponding viscosity parameter being defined by the apparent solid viscosity and the rheological parameter A . In addition, a second term appears in the viscoplastic regime, which can be referred as the compression term with the bulk viscosity coefficient being equal to $\mu_s^{\text{app}}/9B$. Besides the previous quantities already highlighted, it takes into account a second rheological parameter B which can be

interpreted as a compressibility factor. According to Nguyen *et al.*,^[22] the rheological parameters A and B can be empirically modeled as follows:

$$A = \frac{3}{g_s^{6.47}} \text{ and } B = \frac{1}{g_s^{6.94}} - 1. \quad [3]$$

It can be seen that both coefficients are maximal (but finite) when the solid fraction is equal to g_s^t (which corresponds to the start of the viscoplastic regime) and then they exhibit an exponential decay as g_s increases.

The terms μ_s and μ_s^{app} represent the solid viscosity terms in each of the regimes. For low solid fractions, Ishii^[31] postulated that the mixture viscosity of a set of particles can be expressed according to the Power-Law viscosity model:

$$\mu_{\text{mix}} = \mu_l \left(1 - \frac{g_s}{g_s^p} \right)^{-2.5g_s^p} \quad [4]$$

with g_s^p being defined as the random packing limit, which establishes the threshold from which the equiaxed grains create a rigid structure. It is usually expressed in the literature as loose or close packing limit depending on the compaction protocol. In the current study, the loose random packing of spheres of 58.5 pct proposed by Olmedilla *et al.*^[32] has been adopted. It is worth mentioning that the original physical interpretation of this parameter is not particularly complying with the viscoplastic approach proposed in the current study, as the solid phase is considered to become a rigid structure above the packing limit. Nevertheless, g_s^p is required in Eq. [4] to calculate the solid viscosity in the nonviscoplastic regime, and therefore, should be regarded as a fitting constant that affects the evolution of the viscosity in this regime.

Assuming the validity of the mixture rule for the entire simulation ($\mu_{\text{mix}} = g_s \mu_s + g_l \mu_l$), one can determine the corresponding solid viscosity as follows:

$$\mu_s = \frac{\mu_l}{g_s} \left(\left(1 - \frac{g_s}{g_s^p} \right)^{-2.5g_s^p} - (1 - g_s) \right). \quad [5]$$

It is worth mentioning at this point that the transition solid fraction assumed above corresponds to the volume fraction at which the crystals start to become able to sustain tensile loads. This threshold is usually referred to as rigidity point in the literature.^[33] On the other hand, the coherency point is defined as the moment at which the solid fraction is high enough such that bridges between crystals start to form, but no tensile loads can be sustained.^[33] Such a threshold is not established

explicitly but can be identified in the nonviscoplastic regime by the exponential increase in the solid viscosity, given by Eq. [5].

Regarding the viscoplastic regime, once the solid fraction exceeds g_s^t , the solid phase is assumed to exhibit viscoplastic behavior. The apparent solid viscosity generally accepted in the literature takes the form given in the Norton–Hoff model:

$$\mu_s^{\text{app}} = 3K_v \left(\sqrt{3}\dot{\epsilon}_s^{\text{eq}} \right)^{m-1}, \quad [6]$$

where K_v and m are the viscoplastic consistency and the strain-rate sensitivity, respectively. The latter parameter is usually assumed as a fixed value which depends on the material properties. Following the study of Nguyen *et al.*,^[22] it is set as 0.213. On the other hand, the viscoplastic consistency can be calculated by combining the strain-rate tensor proposed by Nguyen *et al.*^[22] and the Norton–Hoff stress–strain-rate relation, yielding

$$K_v = \sqrt{3}^{(-1-m)} \left(\beta \exp \left(-\frac{Q}{RT} \right) \alpha^{1/m} \right)^{-m}. \quad [7]$$

Besides the strain-rate sensitivity defined above and the molar gas constant ($R = 8.31446 \text{ J/mol/K}$), this equation involves additional three material-dependent parameters β , Q , and α , which have been set with the following values based on the experimental trials carried out by Nguyen *et al.*^[22] as 4.98×10^{17} , 257 kJ/mol, and 0.03 MPa, respectively. The authors refer that these constants characterize the deformation behavior of an aluminum alloy in the solid state that is close to solidus and are usually temperature dependent. However, in the current study, they have been assumed as constant throughout the process range. Introducing all assumed quantities into Eq. [7] results in a viscoplastic consistency value of $6.31 \times 10^6 \text{ Pa s}$.

As for the equivalent strain rate presented in Eq. [6], it is given by the following expression

$$\dot{\epsilon}_s^{\text{eq}} = \sqrt{\frac{2}{A} (\dot{\epsilon}_s : \dot{\epsilon}_s) - \left(\frac{2}{3A} - \frac{1}{9B} \right) \text{tr}(\dot{\epsilon}_s)^2}, \quad [8]$$

which again depends on the rheological parameters defined in Eq. [3].

The microscopic phenomena resulting from the solidification process are taken into account by considering exchange terms in the conservation equations. $M_{\ell s}$, $\mathbf{U}_{\ell s}$, $C_{\ell s}$, and $H_{\ell s}$ are the mass, momentum, species, and energy exchange rates between solid and liquid and are outlined in Table II.

The mass-transfer rate (for solidification or melting) is calculated as a function of the specific surface area ($S_{\ell s} = n \cdot 4\pi r^2$), impingement factor ($\Phi_{\text{imp}} = \min [g_l / (1 - \pi\sqrt{3}/8), 1]$), and crystal growth velocity (v_r). The latter quantity determines how fast the solid

interface grows (or shrinks) with solidification (or melting). It is calculated according to the following equation:

$$v_r = \frac{D_l}{r_f(1 - r/r_f)} \frac{c_l^* - c_l}{c_l^*(1 - k)} \quad [9]$$

It can be seen that the difference between the average species mass fraction in the liquid at the interface ($c_l^* = (T - T_f)/m_{\ell s}$) and the volume-averaged liquid mass fraction predicted by the species conservation equation (c_l) is the major driving force for crystal growth.

The momentum exchange term can be caused by mechanical interactions (superscript d) or by phase change (superscript p). $\mathbf{U}_{\ell s}^d$ can be interpreted as the drag force between the two phases, with $K_{\ell s}$ being the drag coefficient. In the current study, $K_{\ell s}$ follows the submerged object approach in the lower solid fraction regime, whereas in the viscoplastic regime the porous medium approach with Kozeny–Carman-type permeability is adopted instead. It can then be written as follows:

$$K_{\ell s} = \begin{cases} 18g_l^2 \frac{\mu_{\ell s} C_e}{d^2} & \text{for } g_s < g_s^t \\ g_l^2 \frac{\mu}{K} & \text{for } g_s \geq g_s^t \end{cases} \quad [10]$$

where the terms $C_e = 10g_s/g_l^3$ and $K = K_0g_l^3/g_s^2$ represent the settling ratio and the overall flow permeability, respectively. K_0 is an empirical parameter that has been set to $d^2/180$, so $K_{\ell s}$ maintains a uniform trend during the entire spectrum of volume fractions.

On the other hand, the contribution to the phase change in the momentum exchange term ($\mathbf{U}_{\ell s}^p$) depends on the average velocity value, given by the parameter u^* (with $u^* = \mathbf{v}_l$ during solidification and $u^* = \mathbf{v}_s$ during melting), and the mass-transfer rate. The product of the two terms corresponds to a momentum force (per unit volume and time) that is added to or subtracted from the corresponding phase momentum during a phase change. A similar mathematical expression is also set for the species source term, as it can be seen in Eq. [18]. The solute exchange caused by the phase change is proportional to the mass-transfer rate, with the constant of proportionality being the equilibrium solid mass fraction, c_s^* . Note that further details about the contribution of the phase change in the momentum exchange term have been given somewhere else,^[17] so only a short description is presented here.

Lastly, the enthalpy exchange term is employed to enforce thermal equilibrium between the phases. Even though two energy conservation equations are considered—and so different temperatures are expected in each phase— $H_{\ell s}$ is set with a very large volume heat-transfer coefficient ($h_c = 10^9 \text{ W/m}^3/\text{K}$) between the phases. Such a procedure is a trade off between trying to accomplish the precondition of thermal equilibrium, and at the same time keeping the numerical calculation results as stable as possible.

Table II. Exchange Terms Used in the Conservation Equations

Mass Transfer:	$M_{\ell s} = v_r S_{\ell s} \rho_s \Phi_{\text{imp}}$	(16)
Momentum Transfer:	$\mathbf{U}_{\ell s} = \mathbf{U}_{\ell s}^d + \mathbf{U}_{\ell s}^p = K_{\ell s}(\mathbf{v}_{\ell} - \mathbf{v}_s) + u^* M_{\ell s}$	(17)
Species Transfer:	$C_{\ell s} = c_s^* M_{\ell s}$	(18)
Enthalpy Transfer:	$H_{\ell s} = h_c(T_{\ell} - T_s)$	(19)

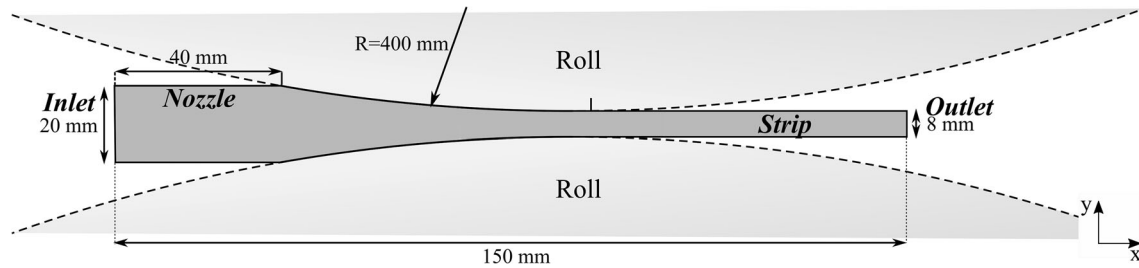


Fig. 1—Schematic representation of the twin-roll continuous casting process.

III. NUMERICAL IMPLEMENTATION

A. Boundary and Initial Conditions

The numerical model presented in this paper has been developed within the OpenFOAM framework. It was originally designed to address exclusively solidification and transport of equiaxed crystals. However, it has now been further improved to account for the viscoplastic regime, whenever the solid fraction is above the transition limit. In fact, the twin-roll casting scenario is a great example where the applicability and robustness of the proposed splitting algorithm can be tested.

The schematic diagram of the geometry discussed here is shown in Figure 1, whereas the boundary conditions used in the simulations are presented in Table III. The geometry replicates a typical twin-roll casting setup for the production of aluminum sheets. The results have been obtained for an inoculated Al-4wt pct Cu alloy ($\cong 2.5$ wt pct). The casting speed is 0.040 m/s and the strip thickness is 8 mm.

Since the width of the sheet is in concept much larger than its thickness, the test case is assumed to be 2D. A mesh composed of 5700 cells was used, which corresponds to an average cell size of approximately 0.85 mm per 0.47 mm. The time step was variable to maintain the convergence and stability of the numerical procedure, but remained in the order of 10^{-4} s a few moments after the start of the simulation.

Melt is injected at the inlet of the domain where a fixed pressure field is specified ($p = 10^5$ Pa). Dirichlet boundary conditions are imposed at the inlet to solid fraction ($g_s = 10^{-3}$, i.e., a practically zero amount), initial crystal diameter ($d = 5 \mu\text{m}$), and liquid and solid species mass fractions ($c_{\ell} = 2.5$ wt pct and $c_s = 0.36$ wt pct, according to the phase diagram). A heat flux boundary condition is imposed on the roll and strip surfaces based on the heat-transfer coefficient

(HTC) of $5.5 \text{ kW/m}^2/\text{K}$ and the reference sink temperature $T_{\infty} = 300 \text{ K}$. The solid and liquid heat capacities have been defined as $c_{P,s} = 766 \text{ J/K}$, and $c_{P,\ell} = 1179 \text{ J/K}$, whereas the solid and liquid thermal conductivities have been defined as $\lambda_s = 153 \text{ W/m/K}$ and $\lambda_{\ell} = 77 \text{ W/m/K}$. The remaining fields not given in Table III are set with homogeneous Neumann boundary conditions.

Attention is drawn to the fact that distinct boundary conditions are set to solid (slip) and liquid (fixed values) phases. This will have an important effect on the outcome as it will be discussed later. Notice also that the heat-transfer coefficient for the heat flux is the same in both the roll and the strip sections. Even though this assumption is generally not precise in practical environments, it has been adopted in the current study to simplify the complexity of the simulation as much as possible.

The present model only considers globular equiaxed crystals. Accordingly, the inoculated Al-4wt pct Cu alloy has been chosen in the current study because of its almost globular equiaxed morphology during solidification. Table IV shows the physical properties and phase diagram parameters of this alloy.

Nevertheless, it is worth noting that in the current study, the effect of gravity is neglected, so the sedimentation of the crystals does not affect the interpretation of the flow dynamics observed during the formation of macrosegregation.

As explained in the next section, two different test cases will be presented. The first is presumably more straightforward as it takes into account equal densities ($\rho_l = \rho_s = 2743 \text{ kg/m}^3$) between liquid and solid and that remain constant with the variation of the temperature. The second test case, on the other hand, increases the complexity of the simulation by assuming different densities between the phases (as defined in Table IV). This should prompt solidification-induced

feeding flows to emerge in regions where solidification is taking place, and affect the local macrosegregation distribution.

IV. RESULTS AND DISCUSSION

In order to simplify the interpretation of macrosegregation formation during twin-roll casting of inoculated Al-4wt pct Cu as much as possible, we start with the presentation of a case where we assume temperature independent and equal densities between liquid and solid. Different parts of the physical mechanisms underlying the twin-roll casting technology are analyzed. Afterward, in a subsequent section, a more complex case is presented where different densities between the phases are considered. The outcome is evaluated and the results are compared against the simpler scenario.

A. Solidification with Equal Densities

1. Cooling and solidification

Solidification starts as soon as the melt gets cooled by contacting the roll surfaces. Typical steady-state results for temperature, solid fraction, and velocity of the melt are illustrated in Figure 2. Note that although the model solves both solid and liquid enthalpy conservation equations, the applied large interphasic heat-transfer coefficient ensures generally the same local temperature for solid and liquid. Thus, only one single temperature is referred to in the following text. Also, the black line on the top snapshot identifies the eutectic temperature line (*i.e.*, 825 K), whereas the black line on the middle snapshot signals the location where the viscoplastic model is triggered (which corresponds to a solid fraction of 0.57). This latter contour line is also presented in most of the subsequent results (besides the first temperature snapshots). On the other hand, the white lines displayed in the snapshot illustrating the liquid velocity magnitude represent the streamlines created by the motion of the crystals.

Starting from a casting temperature of 925 K at the inlet of the domain, the material cools down to around 620 K at the outlet. The eutectic temperature is located slightly downstream of the roll nip location. Below the eutectic temperature, solidification is assumed to be finished. The high cooling rates enforced during the process are a distinctive characteristic of this technology, which commonly leads to a fine-grained microstructure.^[8,9] One can notice that the bulk of the solidification occurs predominantly along a very narrow region where the solid fraction increases rapidly. This takes place mostly in the roll section which means that, besides solidification, the solidifying shells are also being subjected to deformation before the strip leaves the roll nip.

As the solidification progresses, the thickness of the partly solidified shells increases, and they eventually merge. The first contact between the two shells happens at a relatively low solid fraction. However, as solidification proceeds, a single sheet with a roughly uniform solid fraction forms. Although merging happens over a certain distance, it is helpful to refer to a single

impingement point. In the literature, the term ‘kissing point’ is often used to refer to two completely solid shells that meet together. In this paper, we have adopted this expression to identify the point where the transition lines that bound the viscoplastic regimes merge.

Commonly in the literature, the distance between the nozzle and the ‘kissing point’ is defined as the sump depth. As it will be discussed later, both depth and shape of the sump can be greatly influenced by certain operation conditions, which in turn will affect certain characteristics of the sheet. It is worth mentioning that the initial conditions in the test case reported here have been chosen such that no particularly intricate physical mechanisms appear in the results illustrated, and so the relative motion between the two phases caused by the deformation of the mush can be properly investigated. For instance, larger casting speeds, distinct heat-transfer coefficients between walls and phases, or different spatial arrangement of the walls could motivate the appearance of unique flow dynamics in the simulation that would influence the macrosegregation patterns. As a result, the conditions employed in the simulations analyzed here have been kept as simple as possible. Nevertheless, the implications of certain operating conditions on the outcome will be briefly discussed in a subsequent section.

2. Macrosegregation and flow dynamics

Figure 3 shows the distribution of the normalized macrosegregation for the present case. Note that here equal densities of solid and liquid are assumed and thus solidification-induced feeding is neglected. The macrosegregation pattern has been normalized ($c_{mix}/c_0 - 1$) so that the initial alloy composition is given by the value 0, whereas positive or negative macrosegregation is illustrated with positive or negative values, respectively. The main findings observed in this case are the formation of negatively segregated outer layers near the surfaces, followed by positively segregated bands, and a less positively segregated centerline. The origin of such deviations from nominal composition can be explained by analyzing the relative flow between the two phases.

Figure 4 illustrates the velocity of the liquid (top half) and solid (bottom half) for both *x*-component (Figure 4(a)) and *y*-component (Figure 4(b)). It is worth emphasizing that since the results are symmetrical along the longitudinal axis, only half of the entire field distribution is shown. Therefore, Figure 4(a) illustrates the *x*-component of the velocity field for both liquid (top half) and solid (bottom half) phases, whereas Figure 4(b) shows the *y*-component of the velocity for both liquid (top half) and solid (bottom half) phases.

It can be seen that the velocity patterns in both phases look nearly identical. However, there are small but important differences that should be highlighted and that can be more easily perceived by considering the distribution of the relative velocity, as shown in Figure 5.

Figure 5 presents the relative velocity between solid and liquid in *x*- (top half) and *y*-components (bottom half) with the black arrows representing the relative velocity of the flow (defined as $\mathbf{v}_r = \mathbf{v}_s - \mathbf{v}_l$). Note that

Table III. Boundary Conditions for Velocity and Temperature Fields

	Solid Velocity	Liq. Velocity	Enthalpy/Temperature
Inlet	pressure inlet	pressure inlet	925 K
Nozzle	free-slip	no slip	925 K
Roll	free-slip	no slip (0.1 rad/s)	heat flux (HTC = 5.5 kW/m ² /K)
Strip	free-slip	no slip (0.040 m/s)	heat flux (HTC = 5.5 kW/m ² /K)
Outlet	0.040 m/s	0.040 m/s	zero gradient

Table IV. Thermodynamic Properties Used in the Simulation

$\rho_l = 2606 \text{ kg/m}^3$	$c_{p(l)} = 1179 \text{ J/kg/K}$	$\mu_l = 1.3 \times 10^{-2} \text{ kg/m/s}$
$\rho_s = 2743 \text{ kg/m}^3$	$c_{p(s)} = 766 \text{ J/kg/K}$	$T_f = 933.5 \text{ K}$
$\lambda_l = 77 \text{ W/m/K}$	$D_l^{Cu} = 5 \times 10^{-9} \text{ m}^2/\text{s}$	$k = 0.145$
$\lambda_s = 153 \text{ W/m/K}$	$D_s^{Cu} = 8 \times 10^{-13} \text{ m}^2/\text{s}$	$m_{ls} = -344 \text{ K}$

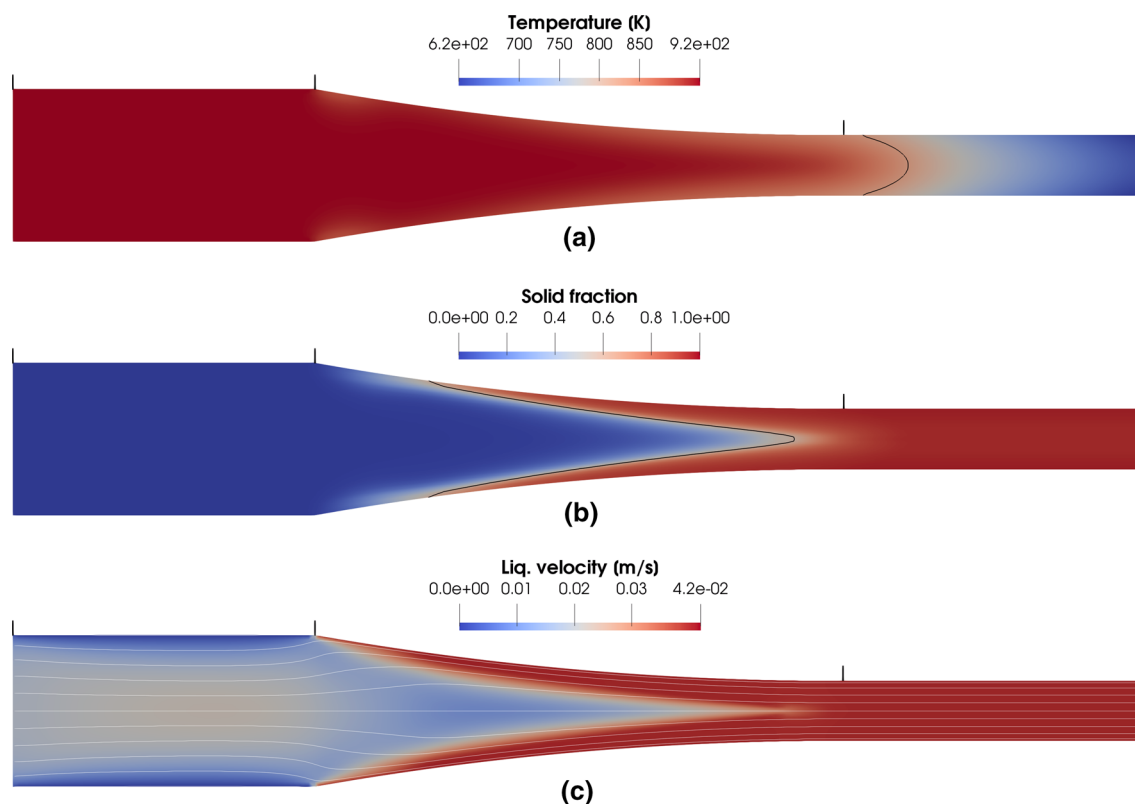


Fig. 2—Steady-state results of (a) the temperature distribution, (b) solid fraction, and (c) liquid velocity magnitude with crystal trajectories in white. Black lines identify $T_{\text{cut}} = 825 \text{ K}$ (top) and $g_s = 57 \text{ pct}$ (middle), respectively. Nozzle, roll, and strip sections are delimited by the vertical markers.

the arrows only express the direction of the relative flow – and not the magnitude—as the arrows have all the same size. Therefore, they allow one to keep a clear perception of the dominant phase in each region of the domain. On the other hand, the magnitude of the relative flow between phases is given directly by the relative velocity distributions. Also, note that the range of the color legend has been reduced so the different characteristics of the flow become clearer.

The whole process of sheet formation by twin-roll casting can roughly be divided into three stages: (i) rapid acceleration of the melt near the wall from zero to roll velocity; (ii) formation of the solidifying, viscoplastic shells along the rolls; and (iii) merging of the top and bottom shells. These three stages are described in more detail in the following:

- (i) The acceleration of the melt starts at the transition from nozzle to roll. Due to the no-slip condition, the

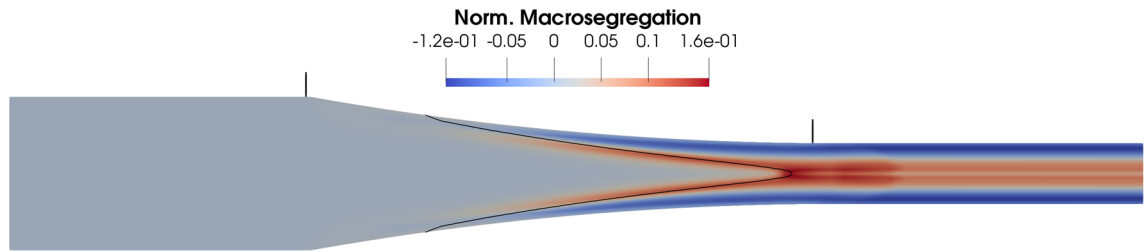


Fig. 3—Steady-state results of the normalized macrosegregation pattern along domain.

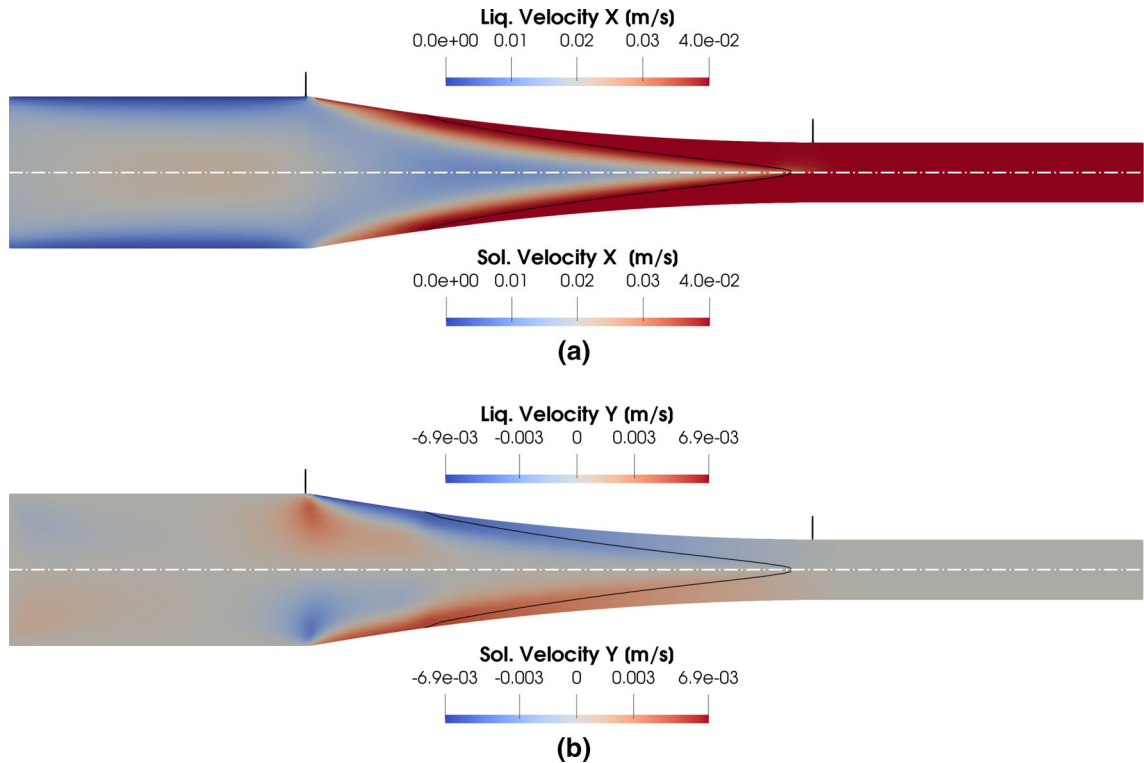


Fig. 4—Velocity of liquid (top) and solid (bottom) for (a) x -component, and (b) y -component.

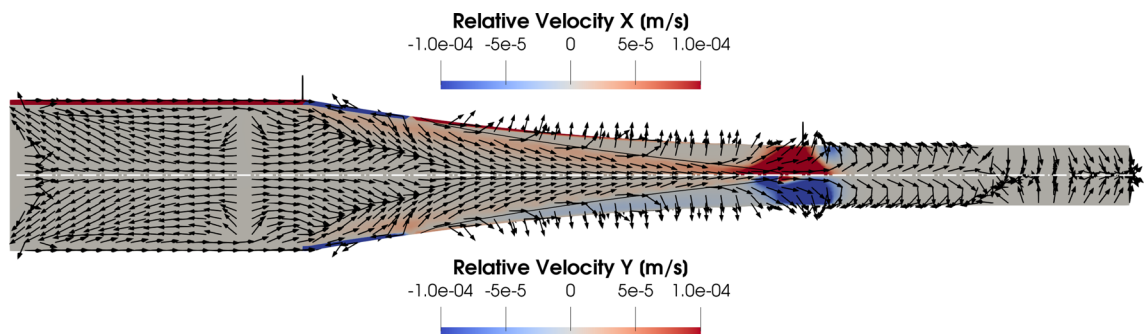


Fig. 5—Relative velocity between solid and liquid (x -direction in top half, y -direction in bottom half). Red areas are where the solid is faster than the liquid (in casting direction for the top half and inward for the bottom half).

melt in contact with the nozzle surface is at rest, whereas the melt in contact with the roll surface moves with casting speed (which has been imposed to the roll surface). This leads to an abrupt speed-up of the liquid phase when it moves from one section of

the domain to the other. This has two direct consequences. Firstly, melt from the center of the domain is dragged toward this nozzle/roll transition point, as shown by the outward flow illustrated in the top part of Figure 4(b)). Second, the relative velocity near the

surface changes from positive values (where the solid phase is faster than the liquid) to negative (see the color change near the surface in Figure 5). Even though at this stage the solid is dragged by the liquid, it does not immediately reach the casting speed imposed to the liquid because of its higher viscosity.

Nevertheless, it is important to underline that, as it can be seen in Figure 3, these phenomena around the transition from nozzle to roll surfaces do not have visible consequences in the macrosegregation pattern.

(ii) The second stage mentioned above is the process of forming the solidifying shells, which takes place in the roll section. It can be seen in Figure 5 that a small surface layer (with slight red color) forms at the beginning of the roll section, where the solid fraction is still below the onset of viscoplasticity. It corresponds to an area where the solid velocity is larger than the liquid both in x (downstream) and y (inward) directions. The reason for this finding is that owing to the reduction in domain thickness and due to the fluid acceleration in the boundary layer close to the rolls, the liquid is generally slowed down in the center of the sump region. As the drag between solid and liquid increases with solid fraction, the crystals end up by being slowed down too because they are carried by the melt. However, since the assumed viscosity in the solid phase is much larger than in the liquid, the solid phase is generally slower than the liquid to decrease its velocity from the imposed casting speed (near the roll surfaces) to the values observed in the sump region. This phenomenon is not related to inertia as here the densities of liquid and solid are assumed to be equal. It is solely due to the fact that the solid phase behaves ‘stiffer’ against any velocity changes. Due to the low amount of solid involved in this phase separation phenomenon, almost no influence can be perceived in the macrosegregation pattern.

As for the solid fractions above the transition limit (*i.e.*, downstream of the black contour line), it can be seen in the top half of Figure 5 that the relative velocity in the casting direction practically vanishes. Tiny differences that show that the solid is slightly faster than the liquid can still be perceived, but they are in the seventh decimal digit. On the other hand, the relative velocity values observed in y -direction (bottom half of Figure 5) are much more significant than in x -direction and indicate that the liquid is moving faster inward compared to the solid. Furthermore, one can notice that the relative flow direction in y -direction is the opposite of what is predicted in the nonviscoplastic regime (see change in direction of the arrows). This clearly demonstrates the change in nature in the flow rheology considered by the simulation. In the viscoplastic regime, the liquid is moving faster than the solid inward because the melt is being squeezed out of the viscoplastic skeleton as the solid is reacting on pulling and deformation.

Such flow dynamics are referred to as compression-induced expulsion, and causes solute-enriched interstitial melt to be transported from the partly solidified shells toward the center. As a result, negative segregated bands

form in the region where deformation of the mush is enforced (mostly near the wall), whereas positively segregated bands start in the locations to where the segregated melt has moved (mostly in the adjacent areas from the negatively segregated bands). Such description can be identified in Figure 3 and explains the origin of macrosegregation there. Furthermore, it can be seen that the negative segregation along the bands near the walls gets gradually stronger as deformation continues until it reaches the roll nip.

(iii) The third stage mentioned above is the merging of the two partly solidified shells. Obviously, the viscoplastic skeletons from both sides are merged under compression. It can be seen in Figure 5 that around the kissing point the magnitude of the relative velocity is the largest. In the bottom half of Figure 5, one can observe that due to compression, liquid is expelled of the solidifying skeleton toward the center and, thus, liquid is perceived to move inward faster than the solid. This phenomenon strengthens the existing composition deviations, especially the positively segregated bands occurring near the center (as it can be seen in Figure 3).

As for the horizontal component of the relative velocity depicted in the top half of Figure 5, the solid is faster than the liquid in the casting direction because the interstitial melt tends to move preferentially upstream—where the resistance of the flow is lower—rather than downstream. Furthermore, since the flow is essentially symmetrical along the longitudinal axis, the relative motion of the flow is exclusively horizontal along the centerline (as the arrows in Figure 5 indicate). This suggests that the sudden velocity increase toward casting speed observed when the solid fraction exceeds the viscoplastic threshold is not fully accompanied by the interstitial melt. Such an occurrence has been found to reduce the number density of crystals along the centerline. In addition, as the increase in the crystals average radius during solidification occurs mainly on the base of the initial melt concentration, c_0 (although segregated melt coming from off-centered areas is also used, but in a smaller amount), a less positively segregated band is formed downstream of the kissing point along the centerline (as shown in Figure 3).

Figure 5 also indicates that the merging-induced compression zone ends right at the roll nip. Interestingly, from the top part of Figure 5, one can observe that directly at the roll nip near the center of the domain the solid moves faster than the liquid, whereas at the periphery the opposite situation occurs and liquid flows downstream faster than solid. Obviously, in the center the solid movability is larger, whereas, at the periphery, the solid is already so stiff that expelling the liquid is easier. The reason for that gets obvious after analyzing Figure 6 where the distribution of the effective solid viscosity (*i.e.*, combination between the solid viscosity in the low solid fraction range, and the apparent solid viscosity in the viscoplastic regime) is shown. One can immediately notice the significant increase in viscosity as solidification proceeds. In fact, at the interface where the viscoplastic regime is employed, the viscosity jumps

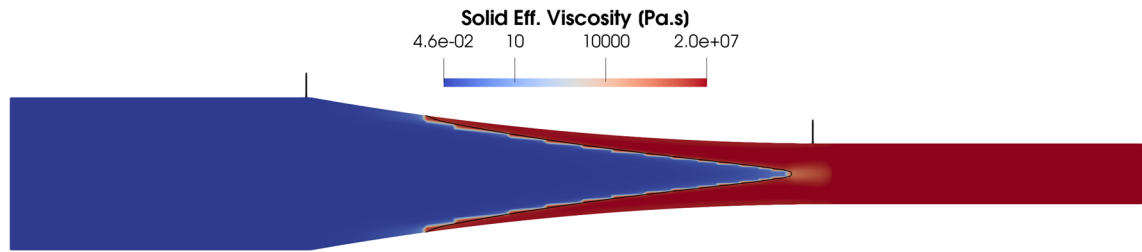


Fig. 6—Steady-state results of the effective solid viscosity, which is a combination between the solid viscosity in the low solid fraction range and the apparent solid viscosity in the viscoplastic regime. Color legend has been scaled for better visualization.

several orders of magnitude. However, it can be seen that the apparent viscosity at the center close to the roll nip is temporarily smaller by three orders of magnitude. This is because the impingement of the two semisolid shells forces the two solid skeletons from both sides from circular to straight horizontal motion. Thus, the effective strain rate of the solid phase increases at the centerline and consequently the apparent viscosity decreases locally according to Eq. [10].

After the roll nip, a small increase in the positive macrosegregation can be identified right at the beginning of the strip section, which then fades away afterward (see Figure 3). At this point, the domain becomes completely horizontal and so no relative flow would be expected purely from the domain constraints. However, as described previously, the coherent structure is being compressed in the roll section, and this flow dynamic is transported to the first part of the strip section. The combination of this relative flow (where liquid is moving faster inward than the solid) with the solidification process that is taking place here explains the strengthening of the positive macrosegregation. Later, the flow dynamics dissipate and the solidification eventually stops because the temperature decreases below eutectic (see Figure 2(a)), which then results in a constant macrosegregation along the strip section.

3. Additional flow details

Note that the behavior of the different phases is based on which phase is the active, governing phase. In the viscoplastic regime, the solid is the dominant phase, and it is being pulled with casting speed in x -direction. This motion is transferred to the whole solidifying coherent skeleton as the apparent solid viscosity is about nine orders of magnitude higher than the solid viscosity below the transition limit (as illustrated in Figure 6).

The fact that the effective solid viscosity exhibits such a considerable increase upon entering the viscoplastic regime results in an enormous rise in material stiffness in x -direction. On the other hand, perpendicularly to the casting direction, the solid fraction decreases to values below the viscoplastic limit, and thus the resulting viscosity is naturally much lower. Such context can explain why the magnitude of the solid velocity slightly exceeds the casting speed, as observed in the bottom half of Figure 7). It suggests that for the solid phase the change in direction due to domain restriction (which becomes narrower in the roll section) is solely carried out by the y -velocity component toward the center, as

the x -component is everywhere equal to the casting speed. A corresponding (extremely small) slip between roll surface and the casting surface is thus expected, especially for the newly formed thin shells. Also, it can be seen in Figure 7 that this induced y -velocity component decreases as the material approaches the nip of the rolls (and so does the magnitude of the solid velocity above casting speed), since the flow is no longer forced to move also inward.

Due to drag, the interstitial liquid also moves with a slightly higher velocity than casting speed, except at the roll surface where it matches exactly the casting speed. As mentioned before, the interstitial liquid is being dragged by the viscoplastic skeleton so that it moves approximately with the same velocity as the solid phase. However, the no-slip boundary condition at the roll surface dictates the liquid velocity there. This description of the melt can be clearly identified in the top half of Figure 7), where the x -component of the velocity is presented.

Note that in the top part of Figure 7 the maximum velocity considered in the color legend is smaller than in the bottom. Thus, the dynamics of the liquid phase are somewhat amplified in the picture (compared to the solid phase) both in the region between the rolls and right after the roll nip. Regarding the liquid velocity increase observed in the latter region, it emerges in a place where expansion forces are found. This phenomenon occurs mainly in order to restore the balance between the phases, after considerable compression forces were enforced around the kissing point and further downstream along the centerline. Such events were explained above, referring to Figure 5. It was also seen that after this point, the relative motion between the phases vanishes, and so both phases move with similar velocity.

B. Solidification with Different Densities

As described in the previous section, the compression mechanism of a semisolid can cause by itself a local increase in solid fraction, which is accompanied by expulsion of liquid in that region. In the current paper, we refer to this mechanism as compression-induced expulsion. However, in contrast to the test scenario reported in the previous section, generally, the solid crystals that form during solidification have a higher density than the original liquid. Therefore, additional material is needed when the solid fraction increases to

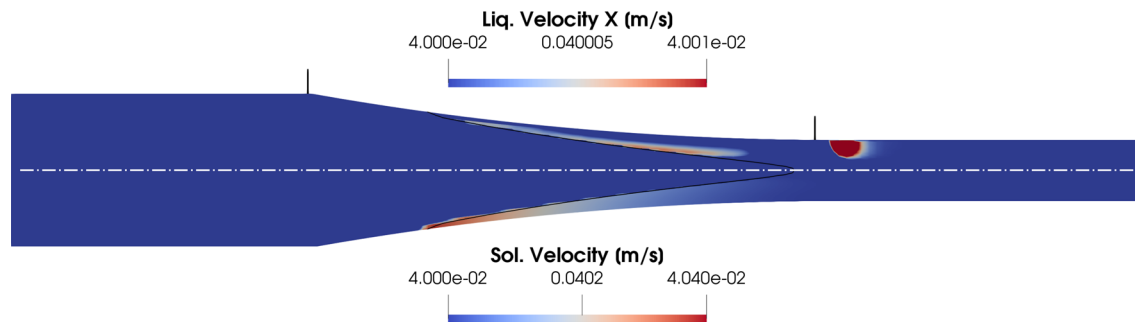


Fig. 7—Steady-state results of x -component of the liquid (top) and magnitude of the solid velocities (bottom), both with data ranges limited to values above casting speed.

feed solidification. This leads to the well-known solidification-induced feeding, which is a flow of either almost exclusively interstitial liquid (called liquid feeding) or liquid transporting crystals (called mass feeding) moving toward the solidifying areas. As solidifying liquid has usually a higher species concentration compared to the solid, one can generally predict that solidification-induced feeding induces positive macrosegregation. This contrasts with the compression-induced expulsion mechanism which generally causes negative macrosegregation to occur. In cases where both solidification and compression happen at the same location simultaneously, the more dominant phenomenon determines whether feeding or expulsion happens predominantly in that region, which then correlates with the positive or negative macrosegregation profile, respectively. Such a scenario where both these mechanisms are considered is analyzed in the present section.

Note that the opposite of the mechanisms mentioned above is also possible, namely melting-induced expulsion and decompression-induced feeding. Melting-induced expulsion leads to negative macrosegregation, whereas decompression-induced feeding leads to positive macrosegregation.

1. Flow differences

If different material densities are considered, the overall picture remains similar although small changes can be detected in the temperature distribution, the solid fraction, and the liquid flow field. In the following, the case with equal densities is referred as Case A, whereas the case with different densities is referred as Case B. In order to discuss the main differences, the x - and y -components of the relative velocities between the two cases are compared in Figure 8. To facilitate the analysis of the different phenomena, different areas of interest have been labeled in the x -component velocity plot with $x_1 - x_6$, and in the y -component velocity plot with $y_1 - y_7$.

Comparison between Case A and Case B allows one to identify some similarities between the two cases. For instance, as discussed in the previous section, in Case A the liquid is abruptly accelerated at the nozzle/roll transition point from zero to casting speed. As the crystals are not ‘feeling’ the imposed velocity directly

(because of the slip condition), they are left behind because drag between solid and liquid is not yet strong enough. This leads to a larger liquid velocity compared to the solid in both components, as observed at areas x_1 and y_1 of Figure 8. At area x_2 , the viscoplastic solid skeleton is pulled with an x -velocity component equal to the casting speed. The liquid, on the other hand, divides the same casting speed that is imposed as a boundary condition at the circular roll surface to both x - and y -components. As a result, the x -velocity component of the liquid close to the surface is lower than in the solid. At area x_3 , the solid is moving faster in x -direction compared to the liquid, because the solid phase behaves kind of ‘stiffer’ than the liquid (due to higher viscosity) and thus is more resistant to the new flow dynamics induced by both the geometrical constraints and the solidification related mechanisms. These phenomena occurring in these four locations are nearly equal in both Case A and B.

On the other hand, an obvious difference between the two cases can be seen in areas y_2 and y_3 . In Case B, the results indicate that the solid moves faster inward than the liquid, whereas in Case A the opposite occurs. In other words, although compression during deformation occurs in both cases, the solidification-induced feeding flow outweighs the compression-induced expulsion in Case B. As a result, the predicted relative velocity in y_2 and y_3 defined in the bottom half of Figure 8(b)) becomes positive, instead of the negative value observed in Figure 8(a)) in the same region. Note that solidification-induced feeding in the viscoplastic regime consists of interstitial liquid only, whereas below the transition, solid fraction crystal motion also contributes to the feeding (at least partly, and for lower solid fractions).

Similarly to Case A, in the second scenario compression can be identified in the region where both viscoplastic shells merge. In Case A, most of the compression region in the roll section shows that the liquid is moving forward slower than the crystals. This means that the interstitial melt is being ejected upstream, but it is not strong enough to overcome the prevailing casting velocity. On the other hand, further downstream, a blue area can be seen near the wall (top half of Figure 8(a)), which corresponds to a region where the melt is moving faster than the solid in the casting direction. Both of these findings can be seen also in Case

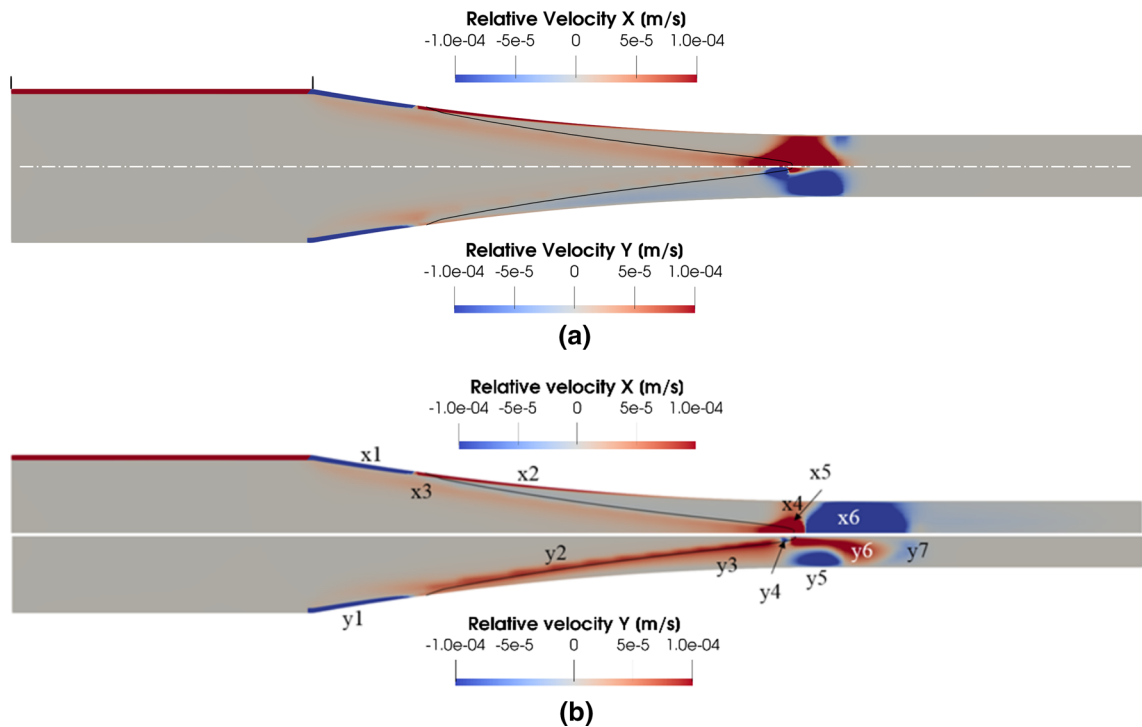


Fig. 8—Relative velocity distribution for the cases (a) with equal densities between solid and liquid (Case A) and (b) for a solid density that has been assumed larger than the liquid (Case B). The top half of each snapshot represents the x -component of the relative velocity, whereas the bottom half represents the y -component. Red indicates areas where the solid is faster than the liquid (in casting direction for the top half and inward for the bottom half).

B. However, in the latter case, a larger blue area (x_6 in Figure 8(b)) appears in the prediction results (where liquid is faster in the x -component than solid) because of the solidification-induced feeding flow.

As regards the area x_4 , the battle between compression- and solidification-induced feeding flows does not reveal a strong dominant mechanism, and so the relative motion is less significant than that in area x_5 . Nevertheless, compression still appears to be the more dominant mechanisms here, which is translated in a faster solid phase compared to the liquid.

Regarding the y -component of the relative velocity, in Case B, the areas y_4 and y_5 , where the liquid is moving inward faster than the solid, are separated, whereas in Case A, the two areas are connected. The area y_5 shows that compression of the solidifying skeleton is expelling liquid not only against casting direction but also inward. On the other hand, the area y_6 (where the solid is moving faster inward than the liquid) is much smaller in Case A than in Case B.

Area y_4 , however, is caused by a different mechanism. As already discussed, the solid along the centerline is rapidly accelerated when the solid fraction increases and the pulling force of the downstream sheet starts to act. This acceleration of the solid results in a depletion of crystals, and thus, liquid is sucked toward the center. However, this effect is marginal. On the other hand, solidification-induced feeding of the last areas that solidify redirects the liquid inward and toward the

casting direction, especially in area y_6 . That is why in Case B, the inward motion of the solid skeleton in this region is now exceeding the liquid inward motion.

Figure 9 shows the magnitude of the relative velocity field for both Case A (top half) and Case B (bottom half) in a delimited region of the domain around the kissing point. The color scale exhibits the entire range of the relative velocity found in the steady-state results. As a consequence, most of the flow dynamics that have been analyzed in details previously are not perceptible in this figure. However, the snapshot allows one to identify the spots near the compression zone where the relative velocity shows obvious differences between solid and liquid. The first spot in the bottom half of Figure 9 depicts an area where the relative velocity occurs due to the compression of the two solidifying shells. A similar spot is observed in Case A (top half of Figure 9), but much stronger as discussed next.

The second downstream spot occurs only for Case B (bottom half of Figure 9) and corresponds to an area where the relative velocity is mostly caused by solidification-induced feeding, which is why it only appears in Case B. It can also be seen that the downstream feeding flow toward the last solidifying areas grows less along the centerline. As discussed above, rapid acceleration of crystals along the centerline into colder regions leads to a solidification based mostly on the initial alloy concentration. Thus, the solid fraction right at the centerline is slightly larger than off-centered locations. This

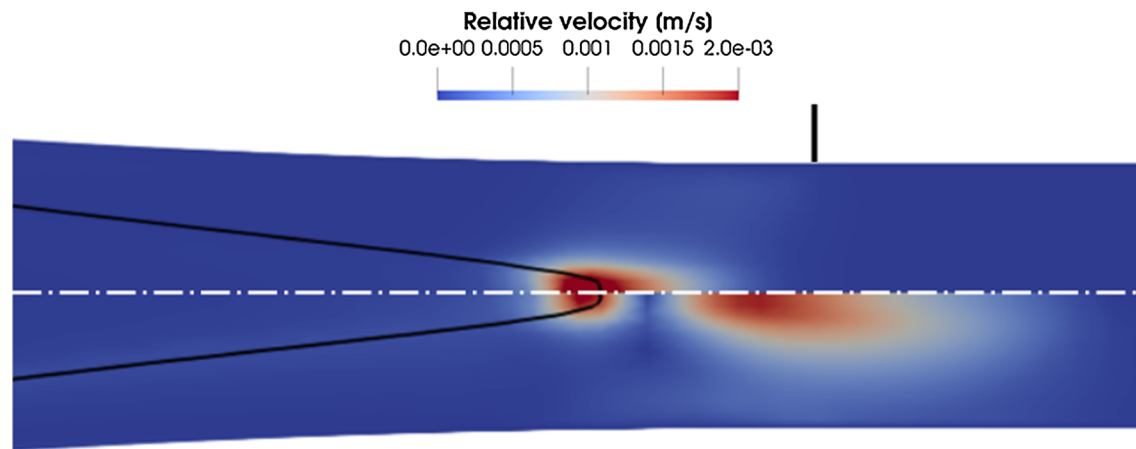


Fig. 9—Magnitude of the relative velocity field for Case A (top half) and Case B (bottom half).

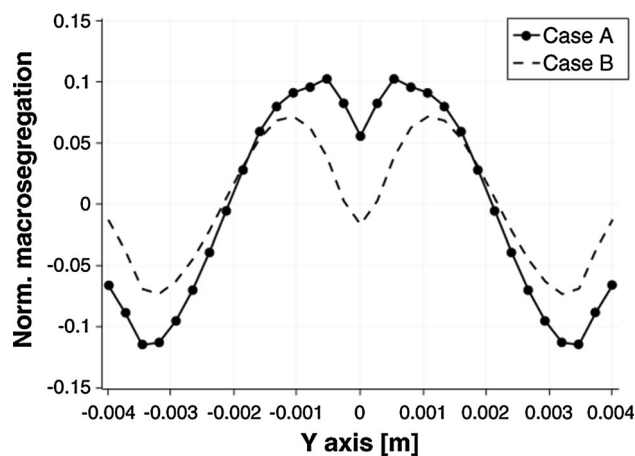


Fig. 10—Final normalized macrosegregation pattern for equal densities (Case A) and different densities (Case B) in fully solidified strip.

redirection of the solidification-induced feeding flow around the center is also the reason for area y_7 in Figure 8(b)) to appear. Note also that the downstream limit of this second spot matches the shape of the eutectic temperature isoline (compare with Figure 2(a)).

2. Macrosegregation differences

Figure 10 shows the two final macrosegregation profiles along the cross section of the strip near the outlet of the domain. It gets obvious that the maximum composition deviations found in Case A are weakened in Case B. This is because, as explained above, solidification-induced feeding and compression-induced expulsion have opposite effects on the formation of macrosegregation and can counteract each other in specific cases. In the scenario where different densities are assumed between liquid and solid (Case B), the effect of compression-induced expulsion on the formation of macrosegregation has been found to be partly weakened by the occurrence of solidification-induced feeding.

Two additional findings have been found rather important and should be discussed. Firstly, notice that in Figure 10, positive surface segregation (thiso-called inverse segregation) is not predicted because the deformation of the solid shells is the most dominant mechanism. Nevertheless, it is worth mentioning that positive surface segregation – specifically at the straight strip section – can be observed at the walls in Case B in the first moments of the simulation, *i.e.*, while the two viscoplastic shells are not yet merged together into one single strip. Such segregation is a consequence of solidification-induced feeding flow and was described and predicted already in the 1970s by Flemings.^[34] However, it turns out that the compression mechanisms that lead to the formation of the negative bands is far more significant and finally no positive surface segregation emerges in the steady-state results.

Secondly, the centerline segregation changes sign: in Case A it is positive, whereas in Case B it is slightly negative. This can be understood by the fact that solidification along the centerline is different from off-centered solidification. Although the liquid surrounding the crystals is dragged by the solid, the horizontal relative velocity suggests that the melt is only partly able to follow the solid phase and so (segregated) melt from off-centered areas are required in the center. That is why Case A has a small positive deviation from nominal composition along the centerline. In Case B, because of the flow needed to feed solidification, the centerline crystals solidify from a melt which comes mostly from the initial, unsegregated melt. As a result, solidification-induced feeding flow is found to weaken the deviations from nominal composition both near the surfaces and in the compression zone (and specifically along the centerline). In addition, as in Case A, compression in the merging zone decreases the crystal number density along the centerline. The combination of both effects results in the formation of a negative centerline segregation in Case B.

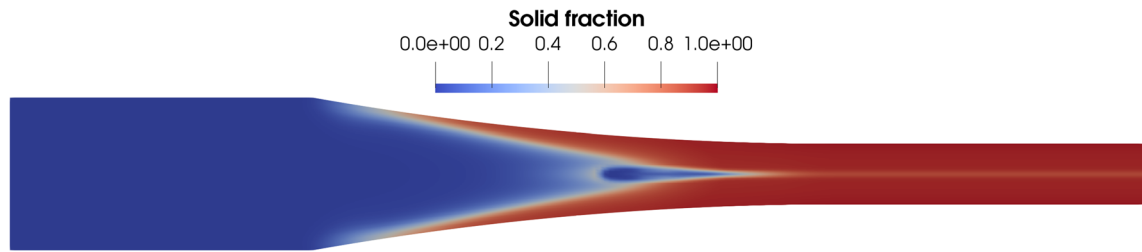


Fig. 11—Steady-state solid fraction distribution in the test case with lower casting speed (28 mm/s) and heat-transfer coefficient at the strip section of $2 \text{ W/m}^2/\text{K}$.

C. Influence of Operating Conditions

As mentioned earlier, the conditions adopted in the test cases replicated here are such that the two solidified shells grow up to a certain size, which is just slightly bigger than half of the final strand width. Therefore, the amount of interstitial liquid that is expelled of the coherent structure when both are pressed together is small.

However, if one were to increase the cooling rates, or decrease the casting speed in the initial conditions, the interaction between the solid shells would be such that additional material—consisting mostly of interstitial liquid—would have to be expelled from the solid skeleton. This inverse relation between the casting speed and the stress levels has also been suggested elsewhere.^[35] When the casting speed is low enough, a backward flow usually develops from the kissing point against casting direction through the sump region. Such a scenario has been shown in Figure 11 where the casting speed was assumed to be 28 mm/s (compared to the previous test cases, where the casting speed was assumed to be 40 mm/s).

This phenomenon results in an area of melting, where solid crystals can gradually disappear. It has already been associated with variations in the local grain structure and centerline segregation.^[11] A reverse flow in the vicinity of the roll nip was also reported in a numerical study by Lee *et al.*^[29] Similarly to the current study, the authors considered viscoplasticity of the semisolid. However, they did not account for segregation, and thus melting was not predicted. On the other hand, even though a similar test case was discussed in a companion paper,^[36] a more thorough analysis of the physical mechanisms underlying recirculation and remelting during thin-roll casting, as well as of the repercussions of the imposed operation conditions on the formation of macrosegregation are intended to be published in the near future.

Note that the heat-transfer coefficient in the strip section in Figure 11 has been set to $2 \text{ W/m}^2/\text{K}$, which is a more realistic value compared to the test cases analyzed in the previous section. Furthermore, the effect of gravity has been evaluated in the simulations but no significant changes have been observed in the final results. These prediction results serve to show the capabilities of the solver described in the present manuscript. Even though the test cases replicated in the previous sections have been simplified for a proper understanding of the macrosegregation results, the

model can be used to predict the outcome of twin-roll casting scenarios with more complex operation conditions.

V. CONCLUSIONS

The following conclusions can be drawn from the presented study on the formation of macrosegregation during twin-roll casting of inoculated (globular solidifying) Al-4wt pct Cu alloys.

- Solidification happens by forming two partly solid shells which merge close to the roll nip.
- Below the viscoplastic transition limit (assumed to be at 57 pct solid fraction), the liquid is the dominant, 'active' phase. On the other hand, above the transition limit, the solid becomes the dominant phase. In other words, fluid dynamics basically governs the flow in the nonviscoplastic regime, whereas in the viscoplastic regime, the solid mechanics dictates the dynamics of the flow.
- In the viscoplastic regime, the two partly solid shells are deforming, and thus compression-induced expulsion of segregated melt leads to the formation of two negative, segregated bands in the outer parts of the as-cast sheet. As a consequence of the compression-induced expulsion mechanism, solute-enriched melt moves toward adjacent areas, and induces the formation of positively segregated bands closer to the center.
- Merging of the two partly solid shells happens over a certain length close to the roll nips. In this area, the partly solid shells are compressed into each other, which strengthens the positive macrosegregation. Furthermore, such phenomenon also leads to an expulsion of melt from that region. It was found that this squeezing out of interstitial liquid takes place mostly in the center because the melt is pressed inward during the deformation of the viscoplastic skeleton. As it approaches the centerline, it moves preferentially upstream because of the lower resistance of the flow. As a result, the as-cast strip reveals a weaker positive deviation (in some cases even negative deviation) from nominal composition along the centerline.
- It is worth noting that the no-slip boundary condition for the solid together with the strong increase in the apparent solid viscosity results in a magnitude of solid velocity that is larger than the casting speed. Thus,

slip of the initial thin partly solid shells along the roll surface is predicted. This is caused by a large ‘stiffness’ of the solid skeleton in the casting direction and relatively soft material behavior toward the center-line.

ACKNOWLEDGMENTS

Open access funding provided by Montanuniversität Leoben. This study was financially supported by the FWF Austrian Science Fund (P28785-N34) which the authors gratefully acknowledge. The authors acknowledge the financial supports by the Austrian Federal Ministry of Economy, Family and Youth and the National Foundation for Research, Technology and Development within the framework of the Christian Doppler Laboratory for Metallurgical applications of Magnetohydrodynamics.

OPEN ACCESS

This article is distributed under the terms of the Creative Commons Attribution 4.0 International License (<http://creativecommons.org/licenses/by/4.0/>), which permits unrestricted use, distribution, and reproduction in any medium, provided you give appropriate credit to the original author(s) and the source, provide a link to the Creative Commons license, and indicate if changes were made.

APPENDIX

Solution Algorithm

OpenFOAM is a C++ toolbox for the development of customized numerical solvers, which are based on the finite volume method (FVM) in order to discretize and solve computational fluid dynamic (CFD) problems. Most of the original solvers provided by OpenFOAM operate on a collocated grid arrangement, which means that all the dependent variables are stored at the cell center. This cell-based formation provides a simple approach with minimal computational effort (since all variables are stored using the same control volume), which makes it suitable for the treatment of complex domains. However, nonphysical pressure oscillations may occur because the pressure gradient does not depend on the pressure in adjacent cells. Nevertheless, this checker-board effect related to the pressure-velocity coupling can usually be suppressed by employing the Rhie-Chow interpolation method.^[37] This makes this arrangement the most widely used among CFD codes.

On the other hand, in some Euler-Euler multiphase flows, the importance of having a more accurate force balance can lead to the preferential use of a staggered arrangement instead. In this framework, since the variables are treated on different grids, the forces can be

treated in a more consistent manner on the cell-faces, which eventually leads to increased stability and accuracy (with possible larger time-steps) in the solution procedure. In OpenFOAM, such upgrade was introduced in 2015, with a formulation that provided a cell-face like pressure-flux staggering on an unstructured mesh. According to the authors, even though the interpolation of the momentum transport terms to the faces reduces the accuracy of this part of the system, this is often offset by the increase in accuracy of the force balance.

In the current study, the face-based momentum equation formulation has been found to be superior to the cell-based one, and thus has been the preferential grid arrangement employed in the simulations presented in this paper.

The implemented algorithm solves a set of differential equations with an iterative segregated approach, which means it evaluates the conservation equations sequentially, and the solution of the linearized system of equations can be used during the subsequent iterative process. Sublooping and iterations are also implemented in order to reach a fair amount of approximation of the results. The numerical configuration adopted in the simulations presented here uses predominantly linear solvers with Gauss-Seidel smoothers.^[38] The exception is the pressure field which is solved using a geometric-algebraic multigrid solver, with a (symmetric) diagonal incomplete-Cholesky smoother.^[38] The corresponding numerical schemes for the discretization of each term in the conservation equations are summarized in Table AI.

Discretization of the general spatial and temporal terms present in the conservation equations have been thoroughly studied in the literature^[39,40] and, thus, will not be reviewed here. In general, the conservation equations deal with nonlinear terms, and so an implicit approach is usually preferred over the explicit method for solving them.

Terms that are treated in an implicit manner always contribute to the matrix coefficients but may or may not contribute to the source vector. Explicit terms, on the other hand, contribute solely to the source vector, which results in a weaker system coupling. This is a key aspect in iterative solvers that are usually used in CFD applications and particularly in multiphase flows like the one considered here.

Table AI. Discretization Schemes for Each Term of the Conservation Equations (ψ Refers to a Generic Variable)

Term	Discretization Schemes
$\partial/\partial t$	Euler implicit
$\nabla\psi$	Gauss linear
$\nabla \cdot (\mathbf{v}_i\alpha_i)$	Gauss van Leer
$\nabla \cdot (\mathbf{v}_i\mathbf{v}_i)$	Gauss limited linear V 1
$\nabla \cdot (\mathbf{v}_i\alpha_i\psi)$	Gauss limited linear 1
$\nabla \cdot (\psi)$	Gauss linear
$\nabla^2\psi$	Gauss linear corrected
$(\psi)_f$	linear

Therefore, the terms in the conservation equations are discretized mainly implicitly, although some particular cases have to be discretized in an explicit manner due to numerical reasons. In this section, details are given specifically on the bulk viscosity related term introduced in Eq. [2].

As referred previously, the principal novelty of the present algorithm resides in the operator which separates the simulation into two regimes, with important differences in the underlying physics involved, and still being able to maintain the stability and accuracy of the solution. Below the transition solid fraction, the top part of Eq. [2] is used for the shear stress (with the solid viscosity being defined by Eq. [10]), whereas above that volume fraction, the bottom part of Eq. [2] is used instead (with Eq. [A1] now being used for the calculation of the apparent solid viscosity). As already referred above, the first term in both regimes of Eq. [2] (related to the deviatoric part of the strain rate) have similar structures, and thus are easily interchangeable as the solid fraction in the domain moves from one regime to the other. In the viscoplastic regime, however, a second term arises, which is a function of the bulk viscosity factor and is characterized by being related to the hydrostatic part of the strain rate. It is defined as follows:

$$(g_s \tau_s^{eff})_{bulk} = g_s \kappa \text{tr}(\dot{\epsilon}_s) \mathbf{I} \quad [\text{A1}]$$

where $\kappa = \mu_s^{\text{app}1}/\eta_B$ is the bulk viscosity factor. This term could be assumed exclusively in an explicit manner in the momentum matrix. However, this could affect negatively the rate of convergence of the solver as soon as the variation of these quantities becomes of the same order or larger than the other terms in the equation. This has soon been found to be not a proper solution since in the viscoplastic regime this term is very significant, and thus ends up by affecting the stability of the solution procedure. A better approach is to manipulate the equation in order to produce a corresponding relation that includes a part that can be handled implicitly, while keeping the other explicit part.

Introducing the namespaces *fvm::* and *fv::* used in OpenFOAM to define implicit and explicit operators, respectively, Eq. [A2] shows how the divergence of the term presented in Eq. [A1] can be defined using a simplified OpenFOAM syntax:

$$\nabla \cdot (g_s \tau_s^{eff})_{bulk} = \text{fvm}::\text{laplacian}(g_s \kappa^3/2, \mathbf{v}_s) - \text{fv}::\text{div}(g_s \kappa^3/2 \text{dev2}(\text{fv}::\text{grad}(\mathbf{v}_s))) \quad [\text{A2}]$$

In Eq. [A2], *fvm::laplacian(.)* returns a matrix in which all the coefficients are based on the finite volume discretization of the Laplacian operator. On the other hand, *fv::grad(.)* returns the gradient of the field inside the parentheses, and *fv::div(.)* returns a field in which the divergence of the field inside the parentheses is evaluated in each cell and is then added to the right-hand side of the system of equations (*i.e.*, to the source term). In addition, the operator *dev2(.)* returns the deviatoric part of the tensor inside the parentheses for compressible flows, which translates to yield the

following relation: $\text{dev2}(A) = A - 2/3 \text{tr}(A) \mathbf{I}$. This is a special form of the Navier–Stokes equations, which is different from classical definition but simplifies calculus.

Proper manipulation of the second term in Eq. [A2] shows that two explicit terms emerge: one given by the Laplacian of the velocity field, and a second that represents directly Eq. [A1]. In theory, the two laplacian terms cancel out and the equation reduces to an expression that represents Eq. [A1]. Nevertheless, this mathematical manipulation has been found to improve stability and accuracy of the simulation. Furthermore, notice that once moved to the LHS of the system of equations, the implicit term becomes negative, which is a requirement to guarantee diagonal dominance.

In spite of the efforts to improve the robustness of the model by means of an implicit treatment of the added terms, some variables still have to be under-relaxed so the changes do not disrupt the stability of computations. In the current study, the most critical case is the effective solid viscosity, which increases by several orders of magnitude during the simulations, and thus, is under-relaxed with a factor of 0.2. As for the conservation equations, an under-relaxation factor of 0.4 for velocities and species has been considered at this stage.

The solution algorithm is based on the PIMPLE approach, which has been widely reported in the literature. The reader is referred to the OpenFOAM user guide^[38] for further information on this topic.

LIST OF SYMBOLS

A, B	Rheological functions
c^*	Equilibrium species concentration [wt.%Cu]
c	Species concentration [wt.%Cu]
c_P	Heat capacity [J/K]
C_s	Settling ratio [m ²]
C_{ls}	Species exchange rate [kg/m ³ /s]
d	Crystal diameter [m]
D	Diffusion coefficient [m ² /s]
g	Volume fraction (-)
g_s^p	Packing limit (-)
h_c	Heat transfer coefficient [W/m ³ /K]
h	Enthalpy [J/kg]
H_{ls}	Energy exchange rate [kg/m/s ³]
\mathbf{I}	Identity tensor (-)
K	Overall flow permeability
K_{ls}	Momentum exchange coefficient (kg/m ³ /s)
K_v	Viscoplastic consistency
k	Partitioning coefficient
M	Strain-rate sensitivity
m_{ls}	Slope of liquidus in phase diagram
M_{ls}	Mass-transfer rate [kg/m ³ /s]
n	Number density [m ⁻³]
p	Pressure (N/m ²)
r	Averaged crystal radius (m)
r_f	Final crystal radius [m]
S_{ls}	Specific surface area [m ⁻¹]
T	Time (s)
T	Temperature [K]
T_f	Melting point of pure metal (Al) [K]

U_{ls}	Momentum exchange rate [$\text{kg/m}^2/\text{s}^2$]
u^*	Average velocity [m/s]
\mathbf{v}	Velocity [m/s]
v_r	Crystal growth velocity [m/s]
x, y	Cartesian coordinates [m]

GREEK LETTERS

ρ	Density (kg/m^3)
μ	Dynamic viscosity (kg/m/s)
τ	Deviatoric stress tensor (N/m^2)
λ	Thermal conductivity [W/m/K]
$\dot{\epsilon}$	Strain-rate tensor ($1/\text{s}$)
ψ	Generic variable
Φ_{imp}	Impingement factor
β	Material-dependent parameter
α	Material-dependent parameter [Pa]

SUB-/SUPERSCRIPTS

app	Apparent
d	Mechanical interactions in momentum exchange
eff	Effective
l	Liquid property
mix	Mixture rule
p	Phase change in momentum exchange
s	Solid property

REFERENCES

1. J.A. Dantzig and M. Rappaz: *Solidification*, 1st ed., CRC Press, New York, 2009.
2. C. Beckermann: Flemings Symp. Boston, MA, 2000.
3. A. Ludwig, A. Vakhrushev, T. Holzmann, M. Wu, and A. Kharicha: *IOP Conf. Ser. Mater. Sci. Eng.*, 2015, vol. 84, p. 012102.
4. A. Ludwig, A. Vakhrushev, M. Wu, T. Holzmann, and A. Kharicha: *Trans. Indian Inst. Met.*, 2015, vol. 68, pp. 1087–94.
5. E.F. Emley: *Int. Met. Rev.*, 1976, vol. 21, pp. 75–115.
6. T. Matsushita, K. Nakayama, H. Fukase, and S. Osada: *IHI Eng. Rev.*, 2009, vol. 42, pp. 1–9.
7. N.S. Barekar and B.K. Dhindaw: *Mater. Manuf. Process.*, 2014, vol. 29, pp. 651–61.
8. M. Ferry: *Direct Strip Casting of Metals and Alloys*, Woodhead Publishing Ltd., Cambridge, UK, 2006.
9. T. Haga, M. Ikawa, H. Watari, K. Suzuki, and S. Kumai: *Mater. Trans.*, 2005, vol. 46, pp. 2596–2601.
10. H. Westengen and K. Nes: *Light Metals: Cast Shop for Aluminum Production*, American Society for Metals, Materials Park, 1984, pp. 972–80.
11. I. Jin, L.R. Morris, and J.D. Hunt: *J. Met.*, 1982, vol. 34, pp. 70–75.
12. D.J. Monaghan, M.B. Henderson, J.D. Hunt, and D.V. Edmonds: *Mater. Sci. Eng. A*, 1993, vol. 173, pp. 251–54.
13. S.A. Lockyer, M. Yun, J.D. Hunt, and D.V. Edmonds: *Mater. Charact.*, 1996, vol. 37, pp. 301–10.
14. B. Forbord, F. Andersson, O. Austevik, J.A. Horst, and I. Skauvik: *Mater. Sci. Eng. A*, 2006, vol. 415, pp. 12–20.
15. A.K. Dahle and L. Arnberg: *Acta Mater.*, 1997, vol. 45, pp. 547–59.
16. J. Ni and C. Beckermann: *Metall. Trans. B*, 1991, vol. 22, pp. 349–61.
17. A. Ludwig and M. Wu: *Metall. Mater. Trans. A*, 2002, vol. 33, pp. 3673–83.
18. M. Wu and A. Ludwig: *Metall. Mater. Trans. A*, 2006, vol. 37, pp. 1613–37.
19. J. Li, M. Wu, J. Hao, and A. Ludwig: *Comput. Mater. Sci.*, 2012, vol. 55, pp. 407–18.
20. J. Li, M. Wu, J. Hao, A. Kharicha, and A. Ludwig: *Comput. Mater. Sci.*, 2012, vol. 55, pp. 419–29.
21. A. Ludwig, A. Kharicha, and M. Wu: *Metall. Mater. Trans. B*, 2014, vol. 45, pp. 36–43.
22. T.G. Nguyen, D. Favier, and M. Suéry: *Int. J. Plast.*, 1994, vol. 10, pp. 663–93.
23. C.L. Martin, D. Favier, and M. Suéry: *Int. J. Plast.*, 1999, vol. 15, pp. 981–1008.
24. O. Ludwig, J.M. Drezet, P. Ménéseès, C.L. Martin, and M. Suéry: *Mater. Sci. Eng. A*, 2005, vols. 413–414, pp. 174–79.
25. O. Ludwig, J.-M. Drezet, C.L. Martin, and M. Suéry: *Metall. Mater. Trans. A*, 2005, vol. 36, pp. 1525–35.
26. C.L. Martin, D. Favier, and M. Suéry: *Int. J. Plast.*, 1997, vol. 13, pp. 215–35.
27. V.D. Fachinotti, S. Le Corre, N. Triolet, M. Bobadilla, and M. Bellet: *Int. J. Numer. Methods Eng.*, 2006, vol. 67, pp. 1341–84.
28. D. Mortensen, H.G. Fjaer, D. Lindholm, K.F. Karhausen, and J.S. Kvalevag: *Light Metals*, 2015, vol. 2015, pp. 1241–47.
29. Y.S. Lee, H.W. Kim, J.H. Cho, and S.H. Chun: *Met. Mater. Int.*, 2017, vol. 23, pp. 923–29.
30. S. Sahoo, A. Kumar, B.K. Dhindaw, and S. Ghosh: *Metall. Mater. Trans. B Process Metall. Mater. Process. Sci.*, 2012, vol. 43, pp. 915–24.
31. M. Ishii: Argonne National Laboratory, Argonne, Illinois, unpublished research, 1977.
32. A. Olmedilla, M. Založnik, and H. Combeau: *EPJ Web Conf.*, 2017, vol. 140, pp. 1–4.
33. J.-M. Drezet, B. Mireux, Z. Szaraz, and T. Pirling: *JOM*, 2014, vol. 66, pp. 1425–30.
34. M.C. Flemings: *Metall. Trans.*, 1974, vol. 5, pp. 2121–34.
35. H. Hadadzadeh, M. Wells, and E. Essadaqi: *TMS*, 2012, vol. 2012, pp. 141–44.
36. C.M.G. Rodrigues, A. Ludwig, A. Kharicha, and M. Wu: *Trans. Indian Inst. Met.*, 2018, <https://doi.org/10.1007/s12666-018-1423-8>.
37. W.L. Rhie and C.M. Chow: *AIAA J.*, 1983, vol. 11, pp. 1525–32.
38. C.J. Greenshields: *OpenFOAM – The OpenFOAM Foundation – User Guide*, 2018. <http://foam.sourceforge.net/docs/Guides-a4/OpenFOAMUserGuide-A4.pdf>.
39. H. Jasak: *PhD Thesis*, University of London, 1996.
40. F. Moukalled, L. Mangani, and M. Darwish: *The Finite Volume Method in Computational Fluid Dynamics - An Advanced Introduction with OpenFOAM and Matlab*, Springer, Cham, 2016.

Publisher's Note Springer Nature remains neutral with regard to jurisdictional claims in published maps and institutional affiliations.